ELECTRODE CURRENT DISTRIBUTIONS IN MGD CHANNELS

NSG-496

Myron A. Hoffman & Gordon C. Oates
Space Propulsion Laboratory
Department of
Aeronautics & Astronautics

CSR TR-66-1 January 1966

Acknowledgement

This work was carried out under the joint sponsorship of NASA Grant NsG-496 (through the M.I.T. Center for Space Research) and Grant No. AF-AFOSR-306-64. The experimental work was carried out with the assistance of Mr. Glenn W. Zeiders and Mr. John J. Karkosak.

ELECTRODE CURRENT DISTRIBUTIONS IN MGD CHANNELS

Myron A. Hoffman* and Gordon C. Oates*

Massachusetts Institute of Technology
Cambridge, Mass.

Abstract

Experimental and theoretical investigations have been made of the current distributions to continuous and segmented electrodes in linear MGD channels. In the experiments the electrodes were subdivided to obtain a measure of the current distribution for various average current densities up to 0.7 amps/cm^2 and Hall parameters up to 5. As expected, current concentrations were measured at the edges of the electrodes. However, the concentrations were less pronounced than those predicted by theories in which constant electrode potential and uniform gas properties are assumed. The experimental results are compared to the predictions of a semi-empirical theory that includes a current density dependent electrode potential. The agreement between experiment and theory in this case is more satisfactory. It is concluded that electrode and sheath voltage drops will tend to limit the current concentrations on the electrodes at least in the current density and Hall parameter regime investigated in this paper.

*Associate Professor of Aeronautics and Astronautics

LIST OF SYMBOLS

$\overline{B}$	Magnetic field
$\overline{E}$	Electric field
$\overline{J}$	Electric current density
β	Hall parameter, $\frac{\sigma B}{e n_e}$
σ	Electrical conductivity
$\overline{E}'$	Electric field as seen by observer moving with fluid velocity = $\overline{E} + \overline{U} \times \overline{B}$
$\overline{e}_B$	Unit vector in direction of magnetic field
$\overline{U}$	Fluid velocity
U	Average axial fluid velocity
ϕ'	Electric potential as seen by observer moving with fluid velocity, i.e., $\overline{E}' = - \nabla \phi'$
ϕ_o	Potential difference found between electrodes as measured in laboratory frame
h	Height of channel
L	Electrode length
x,y	Cartesian coordinates
ξ,η	Dimensionless coordinates. $\xi = \frac{x}{h/2}$, $\eta = \frac{y}{h/2}$
V	Dimensionless electrical potential as seen by observer moving with fluid velocity, i.e., $V = - \frac{\phi'}{\phi_o/2 - UB(\frac{h}{2})}$
W	Complex potential defined by W = Rl. (W) + iV

j_x, j_y Dimensionless electric current components

$$j_{x,y} = \frac{j_{x,y}}{(\phi_o/h - UB)}$$

θ Angle related to Hall parameter = $\tan^{-1}\beta$

e Subscript denoting value of quantity on electrode

A. Introduction

The theoretical advantages to be obtained by operating MGD generators with segmented electrodes have long been recognized. This advantage arises principally because the segmentation of the electrodes allows an axial potential gradient to be sustained which in turn reduces the average Hall current to zero. However, finite segment size introduces several loss mechanisms which reduce the gains predicted for the infinitely finely segmented electrode geometry.

It is theoretically predicted, and observed in practice, that current concentrations occur at the edges of the electrodes. This phenomenon has important practical effects, because the concentration of current causes increased dissipation, and the increased electric fields identified with such concentrations can lead to local current breakdown (arcing) with resultant increased non-uniformity losses and possible electrode erosion.

This paper considers the theoretical formulation of the current and electric field behaviors for several suitable test geometries, and in addition reports the results of some initial small scale experiments.

B. Theory

With the usual assumptions of small magnetic Reynold's number, small charge separation (the plasma assumption), and that the electric current arises from the flow of

electrons only, we may describe the electrical behavior within a d.c. magnetogasdynamic accelerator or generator by the following equations:*

$$\nabla \cdot \bar{B} = 0 \tag{1}$$

$$\nabla \times \bar{E} = 0 \tag{2}$$

$$\nabla \cdot \bar{j} = 0 \tag{3}$$

$$\bar{j} = \frac{\sigma}{1+\beta^2}\left[\bar{E}' - \beta \bar{E}' \times \bar{e}_B + \beta^2 (\bar{E}' \cdot \bar{e}_B)\bar{e}_B\right] \tag{4}$$

Here we have introduced the electric field $\bar{E}' \equiv \bar{E} + \bar{U} \times \bar{B}$, i.e. that electric field seen by an observer moving with the fluid velocity $\bar{U}$. The electrical behavior is most easily described in terms of the variable $\bar{E}'$, so we seek a suitable description of the field behavior of $\bar{E}'$. It is evident immediately that conventional field formulation will be greatly complicated if the plasma properties, σ and β, are allowed to vary spatially, so following Refs. 1, 2 and 3 we restrict our attention to those cases where the effects of spatial non-uniformities are not critical. The regimes of applicability of the present theory will be discussed following development of the pertinent equations.

In what follows we shall restrict our attention to cases in which the magnetic field is applied only in one direction (the z direction) so that the problem may be considered to be two dimensional. With Eq. (2) and the definition of $\bar{E}'$ we then have

$$\nabla \times \bar{E}' = \nabla \times (\bar{U} \times \bar{B}) = (\bar{B} \cdot \nabla)\bar{U} - (\bar{U} \cdot \nabla)\bar{B} + \bar{U}(\nabla \cdot \bar{B}) - \bar{B}(\nabla \cdot \bar{U})$$

*See List of Symbols

With the assumption of two dimensionality, the first operator on the right side vanishes, so that with Eq. (1) there is obtained:

$$\nabla \times \bar{E}' = - (\bar{U} \cdot \nabla)\bar{B} - \bar{B}(\nabla \cdot \bar{U}) \tag{5}$$

In order to obtain an expression for the divergence of the electric field $\bar{E}'$, we take the divergence of Eq. (4) and utilize Eq. (3). We note, also, that for the case considered here of orthogonal electric and magnetic fields, the term $\bar{E}' \cdot \bar{e}_B$ vanishes. In addition, the assumption of small magnetic Reynold's number is equivalent, here, to putting the term $\nabla \times \bar{e}_B$ equal to zero, so that there is obtained:

$$\nabla \cdot \bar{E}' = \beta \bar{e}_B \cdot \nabla \times \bar{E}' \tag{6}$$

The forms given by Eqs. (5) and (6) allow easy investigation of the regime of validity of a potential formulation of the problem. If our investigation into the electric field (and hence current) distribution is restricted to variations occurring in a length that is small compared to an "interaction length", $\frac{\rho u}{\sigma B^2}$, then the problem may indeed be formulated with some accuracy by ignoring the contributions of the right side of Eq. (5). That this should be expected to be the case in a generator is apparent when it is realized that very little magnetic interaction can be expected to occur over a distance of a few electrode segments. Similarly, we will find in what follows that the effect of current fringing at entrance (or exit) from the channel decays approximately exponentially with the

exponent given by the ratio of the axial distance from entrance to the entrance height. Therefore we would expect the potential description to be accurate near the entrance or exit if the interaction length is large compared to the height of the channel, as is to be expected in most working devices.

It is of interest to note that the fluid vorticity does not arise explicitly in Eq.(5). This result indicates that the presence of a boundary layer on the electrodes would not affect the formulation of this problem, provided, of course, that compressibility effects were not of significance. It would be necessary, however, to have a knowledge of the fluid velocity field if it were desired to relate local (laboratory) potential field measurements to the potential field as seen by the fluid. In what follows we assume, for simplicity, that the fluid velocity is uniform across the channel.

Finally, it can be expected that the assumption of a spatially uniform Hall parameter and electrical conductivity will be close to the situation existing in generators operating with little extrathermal ionization, such as combustion generators. It can be expected, also, that these assumptions will be realistic for generators utilizing extrathermal ionization provided they are not operated in the "shorted mode" investigated in Ref. 4.

Within the regime of conditions discussed above, we may

thus write

$$\nabla \times \bar{E}' = 0 \tag{7}$$

and

$$\nabla \cdot \bar{E}' = 0 \tag{8}$$

It is thus apparent that the electric field as seen by the fluid may be described in terms of a potential ϕ', so that transforming to the appropriate dimensionless variables as described in the list of symbols and Fig. 1 we may write

$$\nabla^2 V = 0 \tag{9}$$

In this equation and henceforth it will be understood that the operator ∇ will be taken in terms of the dimensionless variables ξ and η. That is, $\nabla^2 \equiv \frac{\partial^2}{\partial \xi^2} + \frac{\partial^2}{\partial \eta^2}$ The dimensionless electric current density is given in terms of the potential V by the equations:

$$j_x + \beta j_y = \frac{\partial V}{\partial \xi} \tag{10}$$

$$j_y - \beta j_x = \frac{\partial V}{\partial \eta} \tag{11}$$

Formulation in Complex Variables

We shall attempt to obtain the solution as a complex potential W, in terms of the complex variable $\zeta \equiv \xi + i\eta$. It may be assumed that the potential V is the imaginary part of W. If the solution W is found, we may utilize the Cauchy-Riemann conditions to obtain

$$\frac{dW}{d\zeta} = \frac{\partial V}{\partial \eta} + i \frac{\partial V}{\partial \xi} \tag{12}$$

We will be particularly interested in utilizing mapping techniques to obtain the transformation function $\frac{dW}{d\zeta}$, for it can be seen that if a mapping is found that transforms the constant potential (V) lines in the ζ plane into horizontal lines in the W plane, then with Eqs. (10)-(12) we may obtain the electric current distribution without need of integration.

Boundary Conditions

The most obvious idealization to apply to the boundary condition to be found on an electrode is that of constant electrical potential along the electrode surface. The validity of such an idealized description is limited by several effects, principal among which are the effects of finite conductivity of the electrode and of electrode voltage drops. Both these effects can be expected to be somewhat current dependent, so that the large variations in current density predicted by the idealized boundary condition mentioned above could, in fact, be expected to induce a non-constant potential along the electrode boundary, as seen by the gas just external to the electrode sheaths. Rogers [5] attempted to account for such effects with a semi-empirical theory that required machine computation. His predictions have been included for comparison in the figures. In what follows we use the simple boundary condition that V = const. on electrodes, but it must be remembered in the interpretation of the data that

particularly near the predicted current singularities we can expect the current densities to be modified from those predicted by the idealized theory.

The requirement on the insulator that there be no current perpendicular to the boundary leads through Eqs. (10) and (11), to the requirement that the constant V lines intersect the boundary at an angle of $\Theta \equiv \tan^{-1}\beta$ from the perpendicular (Fig. 2).

It is apparent from Fig. 2 that the transformation from the real plane to the desired W plane is conceptually very straightforward, and several geometries have already been considered [1,2,3] using this technique. In what follows we will select several special cases in order to help interpret the experimental results obtained. As discussed previously, the current distribution may be obtained directly from the transformation function $\frac{dW}{d\zeta}$, and in addition, several other desired quantities may be obtained directly from the complex potential or its derivative by appropriate use of the boundary conditions and Eqs. (10), (11) and (12). Several quantities of interest are listed below,

$$j_x = \frac{1}{1+\beta^2}\left[I_M.\left(\frac{dW}{d\zeta}\right) - \beta\, R_L.\left(\frac{dW}{d\zeta}\right)\right]$$

$$j_y = \frac{1}{1+\beta^2}\left[R_L.\left(\frac{dW}{d\zeta}\right) + \beta\, I_M\left(\frac{dW}{d\zeta}\right)\right]$$

$$(j_x^2 + j_y^2) = \frac{1}{1+\beta^2}\ \frac{dW}{d\zeta}\left(\overline{\frac{dW}{d\zeta}}\right)$$

where $\overline{\frac{dW}{d\zeta}}$ is the complex conjugate of the quantity $\frac{dW}{d\zeta}$.

$$(j_y)_e = \frac{1}{1+\beta^2}\left(\frac{dW}{d\zeta}\right)_e$$

$$\int_1^2 (j_y)_e \, d\xi = \frac{1}{1+\beta^2}\left[W_2 - W_1\right]_e$$

Example Solutions

Several simple solutions will be given here because of their usefulness in interpreting the experimental data. It may be noted that the complex notation and list of formulae given above may be applied to the several cases considered in Refs. 2 and 3 with the gain of some simplicity of solution and interpretation of the results.

Semi-Infinite Electrodes

Fig. 2 indicates the necessary transformation from the ζ plane to the W plane for the case of entrance to a pair of semi-infinite electrodes. Straightforward application of the Schwarz-Christoffel theorem (utilizing the intermediate "z" plane) leads to the following transformation function

$$\frac{dW}{d\zeta} = z\,(z+1)^{-\left(\frac{1}{2}+\frac{\theta}{\pi}\right)}(z-1)^{-\left(\frac{1}{2}-\frac{\theta}{\pi}\right)} \qquad (13)$$

in which $z = e^{\frac{\pi}{2}(\zeta+1)}$.

For ease of integration we substitute $\frac{\theta}{\pi} = \frac{1}{n}$ and

$$y = \left(\frac{z - 1}{z + 1} \right)^{\frac{n-2}{2n}} \equiv \left\{ \tanh \frac{\pi}{4} (\zeta + i) \right\}^{\frac{n-2}{2n}}$$

so that Eq. 13 becomes

$$\frac{d W}{d y} = \frac{2}{\pi} \left(\frac{2n}{n-2} \right) \frac{y^{\frac{4}{n-2}}}{1-y^{\frac{2n}{n-2}}} \qquad (14)$$

Integration in closed form can easily be obtained for certain particular values of n. The results of several such integrations that were of use in interpreting the experimental data are summarized in Table I. It may, also, be noted that the normal current distribution on the electrodes can be obtained from

$$\left(j_y \right)_e = \frac{\frac{1}{2}}{1 + \beta^2} \left[\left(\tanh \frac{\pi \xi}{4} \right)^{-\frac{1}{2}} + \left(\tanh \frac{\pi \xi}{4} \right)^{+\frac{1}{2}} \right] x$$

$$\left(\tanh \frac{\pi \xi}{4} \right)^{\pm \frac{1}{n}} \qquad (15)$$

in which for an accelerator the $(+ \frac{1}{n})$ corresponds to the anode case and the $(- \frac{1}{n})$ corresponds to the cathode case, the reverse being true in the generator case.

Finite Length Electrode Pair

The geometry to be considered is illustrated in Fig. 3, and it is found by again applying the Schwarz-Christoffel theorem that the transformation function is:

$$\frac{d\,W}{d\,\zeta} = K\,z\,\left[(z+1)(z-z_2)\right]^{-\left(\frac{1}{2}+\frac{\Theta}{\pi}\right)}\left[(z-1)(z-z_5)\right]^{-\left(\frac{1}{2}-\frac{\Theta}{\pi}\right)} \tag{16}$$

in which

$$z = e^{\frac{\pi}{2}(\zeta+i)}$$

$$z_2 = e^{\pi\frac{L}{h}}$$

$$z_5 = -\,e^{\pi\frac{L}{h}}$$

L = electrode length

K = constant of proportionality

This expression may be used in the form given, to calculate the current density, but it can not be integrated in closed form. The constant of proportionality K is not easily obtained because it requires integration of the equations in order to be determined. However, the current distribution can be numerically integrated and normalized using the total current so obtained. This procedure was followed in comparing experiment to theory in the segmented electrode case.

In order to normalize the current distributions in the continuous electrode case, use was made of the fact that the electrode length was much greater than the electrode

height. Thus, it can be verified that Eq. (16) is readily expanded about $\xi = 0$ in a series of terms of ascending powers of $e^{-\frac{\pi}{2}\frac{L}{h}}$. It follows that for channel lengths appreciably greater than the channel height the mutual interaction of the inlet and outlet disturbances is negligible. For this reason the total current to each electrode was obtained by simply adding the contribution from the anode and cathode up to length $\frac{L}{2}$ as given by the expressions in Table I. The result, of course, is that only the inverse hyperbolic tangent terms contribute to the total current so obtained. The current to the individual subdivisions was obtained by direct application of the results shown in Table I.

C. Experiments

1. Experimental Facility

The experimental facility shown in Fig. 4 consists of an arc plasma source and a graphite plenum surmounted by a boron nitride test section. The primary test gas is fed directly through the arc where it is heated to several thousand degrees Kelvin. The secondary test gas is preheated to about 1000° K in a pot of molten lead. Also immersed in the lead pot is a stainless steel boiler filled with potassium. A controlled amount of potassium is injected through a choked orifice into the secondary gas stream which is mixed with the primary gas stream in the plenum.

The seeded test gas then flows up through the plenum and into the test section.

For the tests to be described the total gas pressure in the test section was approximately one atmosphere. The detailed experimental conditions and gas composition for each run are listed in Table II.

A magnetic field of up to 10,000 gauss was applied across the test section during the tests. Adjustment of the magnetic field strength was the principal means by which the Hall parameter, β, was varied during a run.

2. Segmented Electrode Experiments

Initial experiments were run on boron-nitride test sections employing three pairs of tantalum electrodes as shown in Fig. 5. Each electrode pair had a length to channel height ratio of 0.5, with equal size insulators in between. A separate set of batteries was used to apply an equal voltage to each electrode pair. The center electrode pair of each test section was further subdivided to permit measurement of the current distribution.

Probes made of .020 inch tantalum wire were placed across the test section (in the B field direction) at the locations indicated by the small circles. These probes allowed measurement of the transverse and axial voltages in the free stream as well as the electrode voltage drops.

Typical voltage profiles across the test section are shown in Fig. 6. Note that the data points have been

connected with straight lines in lieu of more complete information on the exact voltage distribution. The linear voltage profile for Run IA indicates a uniform free stream electrical conductivity. On the other hand, Runs IC and IE exhibit a higher conductivity in the center of the flow, indicating a hot core flow.

In all cases the electrical conductivity listed in Table II has been calculated based on the average electric field in the free stream. These values of conductivity are almost two orders of magnitude above the equilibrium values for the measured gas temperatures, indicating the probability of some non-equilibrium ionization.[6]

In test section I, the center electrode was subdivided into three equal parts. The currents measured are plotted in Fig. 7 for each subdivision. Also plotted is the constant electrode potential theory for a single electrode pair. This can be shown to be close enough to the three electrode pair geometry used, to provide a valid comparison.

The current can be seen to be divided approximately as the theory predicts for a Hall parameter, $\beta = 0$. However, as the magnetic field is increased, the strong concentration of the current on subdivision 1 predicted by the theory does not occur. For Run IA where pure argon plus seed potassium was used, the current distribution varied little with increasing β. For Runs IC and IE, where nitrogen was added, the effect of β on the current distribution is somewhat more pronounced.

The overall effect of the nonuniformity of the current due to finite electrode segmentation is to increase the internal resistance of the test section or MHD device. The calculated internal resistance for the experiments, based on the free stream voltage drops, is shown in Fig. 8. There is substantially less increase in internal resistance with β than predicted by the theory, due primarily to the much less severe concentrating of the current in the experiments.

3. Continuous Electrode Experiments

In order to obtain more detailed information about the current concentrations, a new test section shown in Fig. 9 was constructed[7]. It employed a continous electrode of length to channel height ratio, $L/h = 3.2$. This electrode length to height ratio is sufficiently large to leave the duct exit current distribution essentially undisturbed by entrance effects.

The trailing edge of one electrode was finely subdivided into four small pieces to permit a detailed measurement of the current distribution at the duct exit. This yielded about two and a half times more resolution than test section I. As in the other test sections, probe wires were used to measure the free stream and electrode voltage drops.

Typical voltage distributions across the channel for constant total electrode current are shown in Fig. 10.

The free stream electrical conductivity is seen to be quite uniform. The values of the conductivity listed in Table II and the internal resistance values plotted in Fig. 11 are both based on the free stream voltage drops. The conductivities are this time about an order of magnitude above the theoretical equilibrium values, indicating the likelihood of a small amount of non-equilibrium ionization.

The measured current to each subdivision is shown as a function of β in Fig. 12 for Run IIIA. While the currents to subdivisions 2, 3 and 4 are only slightly different from the theory, the current to subdivision 1 is substantially below the theoretical prediction. This result is in complete agreement with the results of the segmented electrode tests.

The results for a Hall parameter of 1.0 are cross-plotted as a function of the subdivision location in Fig. 13. The semi-empirical theory of Rogers[5] has been included for comparison purposes. This modification of the theory which includes a dependence of the electrode potential on the normal current density shows improved qualitative agreement with experiment.

The reduced magnitude of the current concentrations in these experiments is reflected once again in the internal resistance variation with β shown in Fig. 11. This trend compares quite well with the data of Fig. 8 for the segmented electrodes.

In all these experiments the current was clearly distributed over the entire electrode surface. However, we have no direct evidence to indicate whether it was a truly diffuse current or multiple arc fingers through the boundary layer. The presence of a single large arc spot such as observed by Denison and Ziemer[8] with cold electrodes seems highly unlikely.

The electrode drops at the cathode and anode were estimated by extrapolating the free-stream electric field to the wall as indicated by the dashed lines in Fig. 12. These values, plotted as a function of β in Fig. 14, show an interesting trend. For both Runs A and G, the electrode drop on the anode increased sharply with increasing magnetic field, while the drop on the cathode tended to decrease. No explanation for this effect can be offered at this time. It may be noted in passing that the component of the Lorentz force perpendicular to the electrode was away from the anode and into the cathode in both runs. However, the magnitude of this effect does not appear to be large enough to cause a change in the boundary layer of the required magnitude.

D. Conclusions

The current concentrations measured at the edges of segmented and continuous electrodes are substantially less pronounced than those predicted by a constant electrode potential theory. A semi-empirical theory including

a current-dependent electrode potential shows reductions in the current concentrations similar to those in the experiments. It therefore appears that electrode voltage drops will tend to limit the current concentrations in the average current density range up to at least .7 amp/cm^2 at Hall parameters up to 5, and possibly higher in both parameters. This implies that operation of an MHD generator in a distributed current mode should be possible in these current ranges.

References

1. Podolsky, B. and Sherman, A., "Some Aspects of the Hall Effect in Crossed Field MHD Accelerators," ARS Preprint 1531-60, December 1960.
2. Hurwitz, H., Jr., Kilb, R. W. and Sutton, G. W., "Influences of Tensor Conductivity on Current Distribution in an MHD Generator," J. Appl. Phys. 32, 205-216, 1961.
3. Witalis, E. A., "Performance of a Segmented Electrode MHD Generator for Various Electrode-Insulator Length Ratios," to be published in J. Nuclear Energy, Part C, 1965.
4. Kerrebrock, J. L., "Segmented Electrode Losses in MHD Generators with Nonequilibibrium Ionization II," AVCO-Everett Research Report 201, January 1965.
5. Rogers, J. W., "A Theoretical Investigation of the Inlet Current Distribution in an MHD Channel," S. M. Thesis, Massachusetts Institute of Technology, June 1964.
6. Kerrebrock, J. L. and Hoffman, M. A., "Nonequilibrium Ionization Due to Electron Heating," AIAA Jour. 2, 1072-1087, 1964.
7. Karkosak, J. J., "Experimental Investigation of Exit Effects on Current Distribution in an MHD Channel," S. M. Thesis, Massachusetts Institute of Technology, January 1965.

8. Denison, M. R. and Ziemer, R. W., "Investigation of the Phenomena in Crossed-Field Plasma Accelerators", AIAA Paper No. 63-378, August 1963.

TABLE I

NOTE: In every case, $x = x_n = \left\{ \tanh \frac{\pi \xi}{4} \right\}^{\frac{n-2}{2n}}$

Also, for the accelerator configuration, have

- for anode
+ for cathode

} where $\mp$ signs occur

n	Corresponding β	Experimental β with which compared
6	$\frac{1}{\sqrt{3}} \approx 0.577$	0.58
4	1	-
3	$\sqrt{3} \approx 1.73$	1.7
$\frac{8}{3}$	$\tan^{-1} \frac{3\pi}{8} \approx 2.42$	2.4

n	$(W - W_{entrance})_e$
6	$\frac{2}{\pi} \left[\tanh^{-1} \left(\frac{3x}{2 - x + 2x^2} \right) \mp \sqrt{3} \tan^{-1} \frac{\sqrt{3}x}{2 + x} \right]$
4	$\frac{4}{\pi} \left[\tanh^{-1} x \mp \tan^{-1} x \right]$
3	$\frac{2}{\pi} \left[\tanh^{-1} \left(\frac{3x(1+x^2)}{1 + 4x^2 + x^4} \right) \mp \sqrt{3} \tan^{-1} \frac{\sqrt{3}x}{1 - x^2} \right]$
$\frac{8}{3}$	$\frac{4}{\pi} \left[\tanh^{-1} x + \frac{1}{\sqrt{2}} \tanh^{-1} \frac{\sqrt{2}x}{1 + x^2} \mp \left\{ \tan^{-1} x + \frac{1}{\sqrt{2}} \tan^{-1} \frac{\sqrt{2}x}{1 - x^2} \right\} \right]$

TABLE II Experimental Conditions for Each Run

	Three electrode pairs		
Run number	IA	IC	IE
Mode	Gen.	Accel.	Gen.
Gas mole fractions: Argon	.99	.77	.77
Helium	-	-	-
Nitrogen	-	.22	.22
Potassium	.007	.006	.009
Gas temperature (avg.)(^{o}K)	1000	1350	1500
Electron temp. (avg.)(^{o}K)	800	830	(850)
Gas velocity (avg.)(m/s)	25	40	40
Total voltage (avg.)(volts)	26	35	48
Total current (amps)	.013	.55	.80
Current density(avg. j)(a/cm^2)	.011	.48	.70
Exper. σ_∞ (B = 0)(mhos / cm)	.002	.06	.06

	Continuous Electrode		
Run number	III Z	III A	III G
Mode	Accel.	Accel.	Gen.
Gas mole fractions: Argon	-	-	-
Helium	.88	.88	.88
Nitrogen	.11	.11	.11
Potassium	.003	.003	.003
Gas temperature (avg.)(^{o}K)	1550	1660	1680
Electron temp. (avg.)(^{o}K)	1280	1340	1340
Gas velocity (avg.)(m/s)	100	100	100
Total voltage (avg.)(volts)	80	60	60
Total current (amps)	.80	.80	.80
Current density (avg. j)(a/cm^2)	.10	.10	.10
Exper. σ_∞ (B = 0)(mhos / cm)	.009	.009	.009

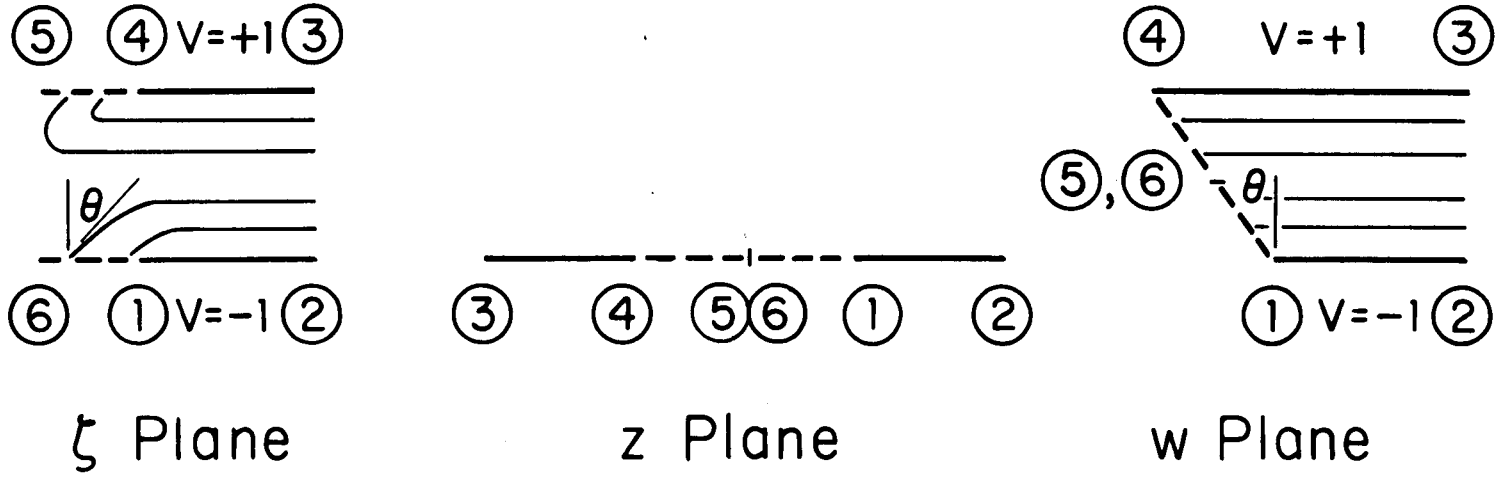

Fig. 2. Conformal transformations; semi-infinite electrode pair

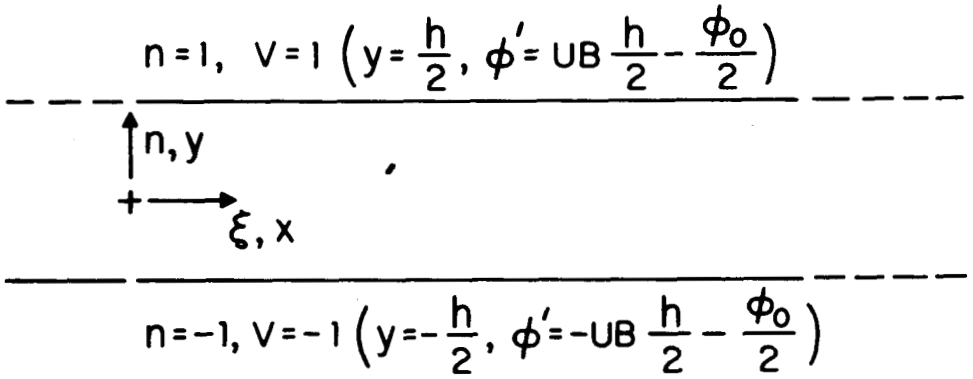

Fig. 1. Coordinates and electrode potentials

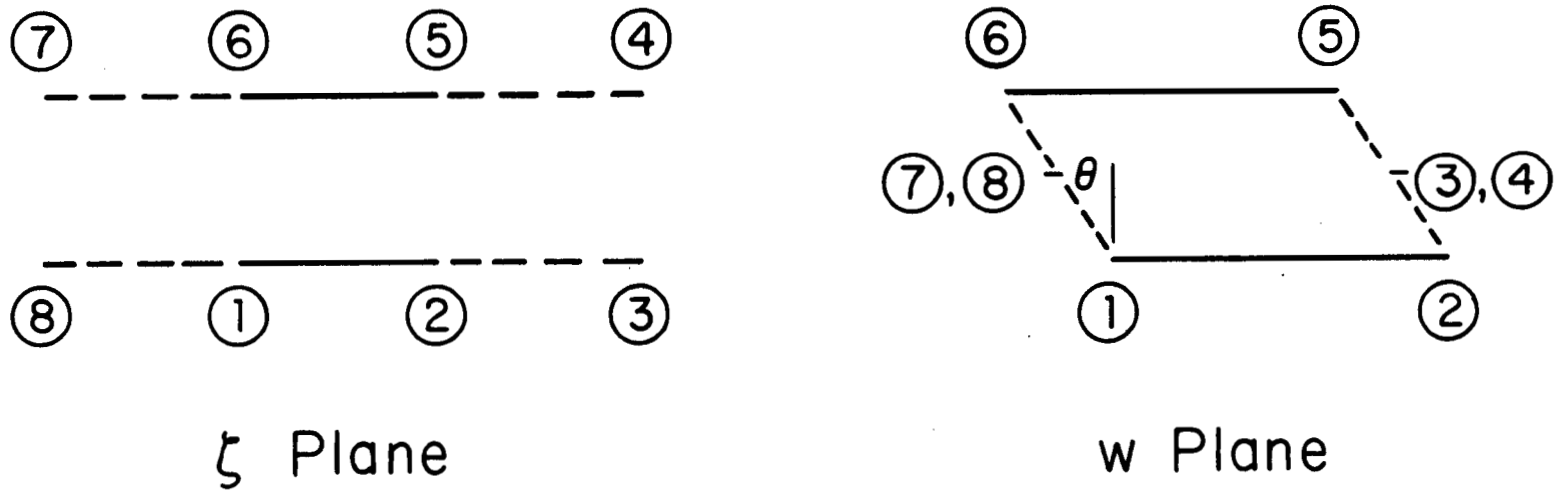

Fig. 3. Conformal transformation; finite electrode pair

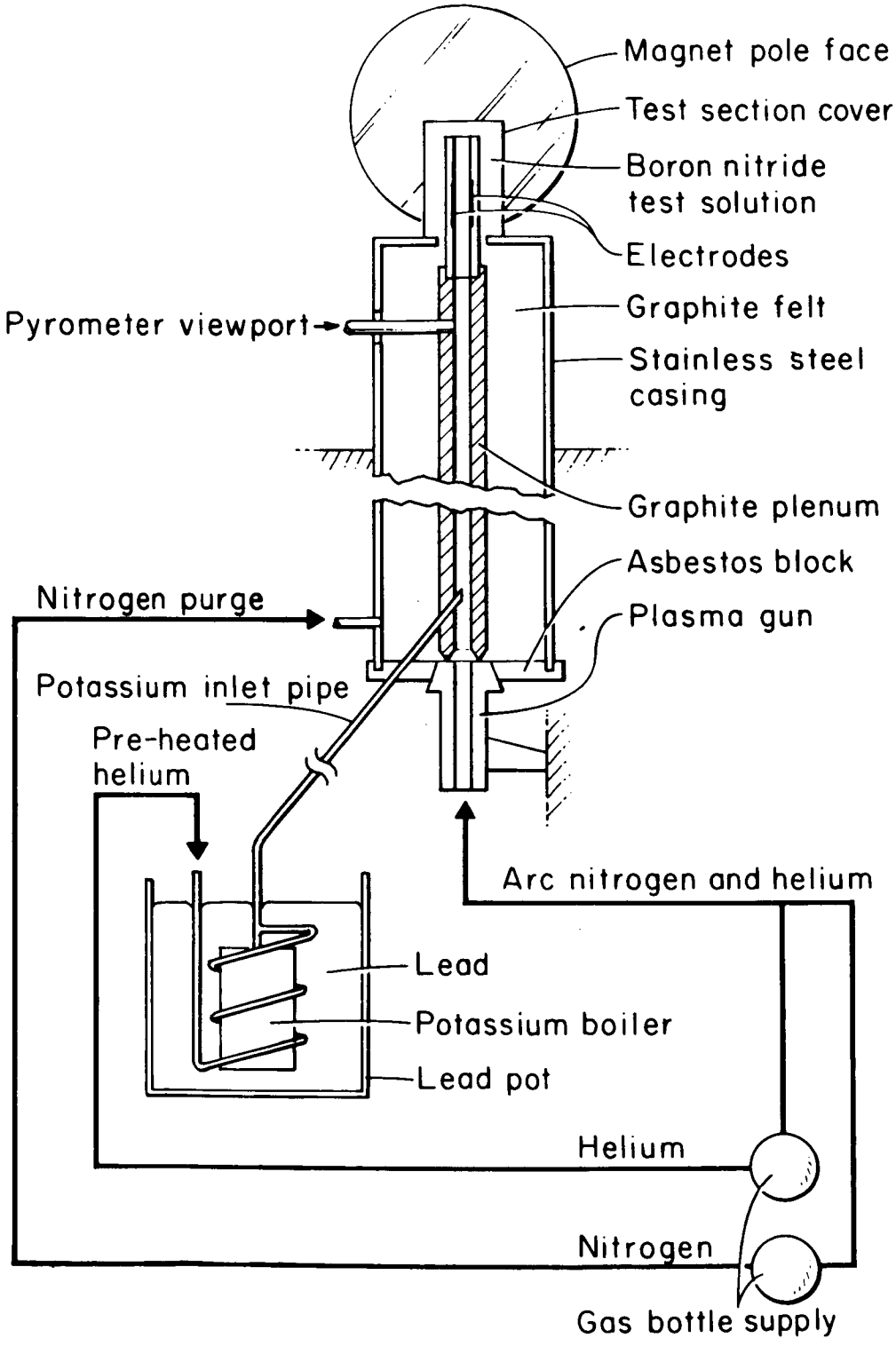

Fig. 4. Experimental facility for small scale electrode tests

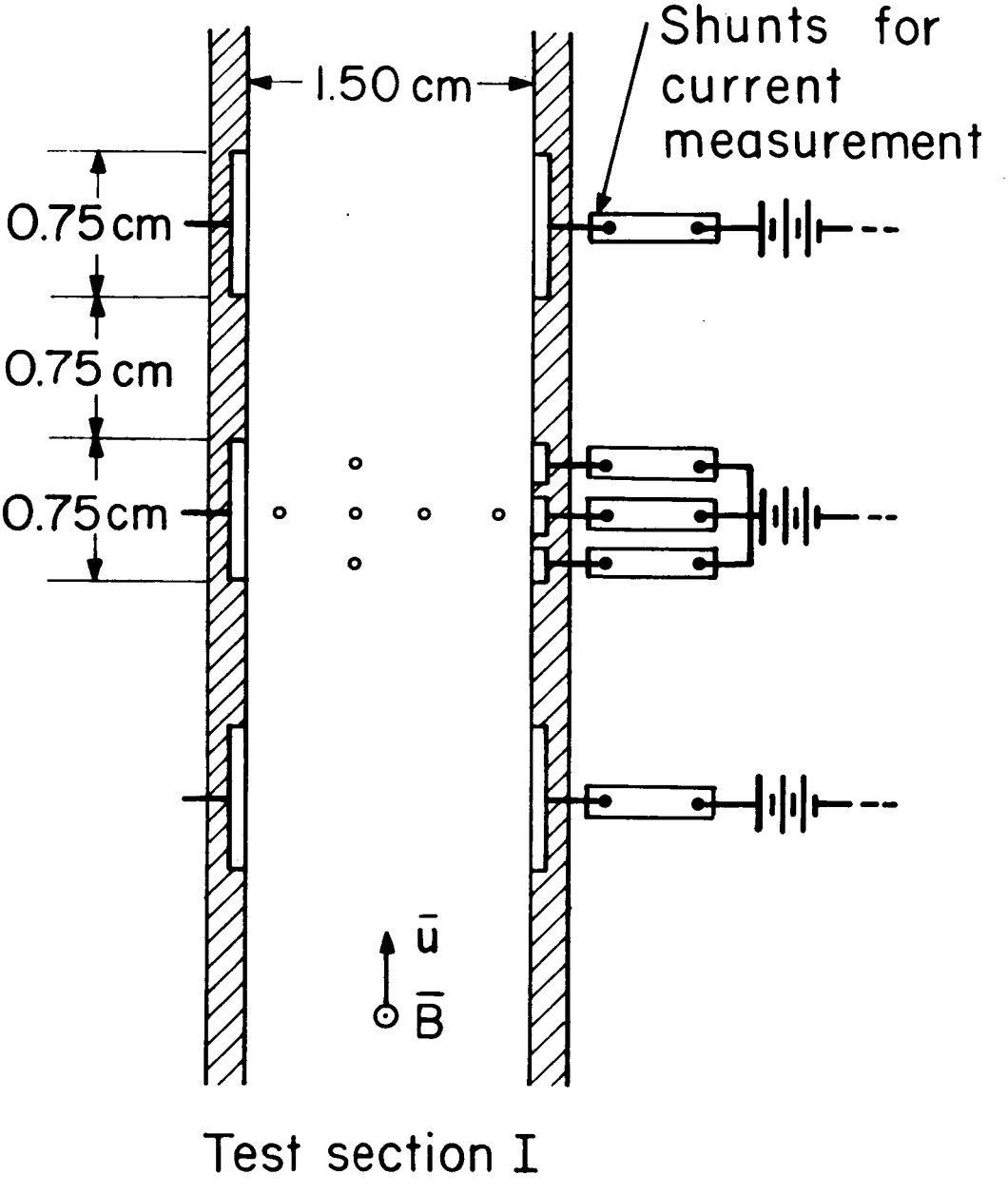

Fig. 5. Segmented electrode test section I

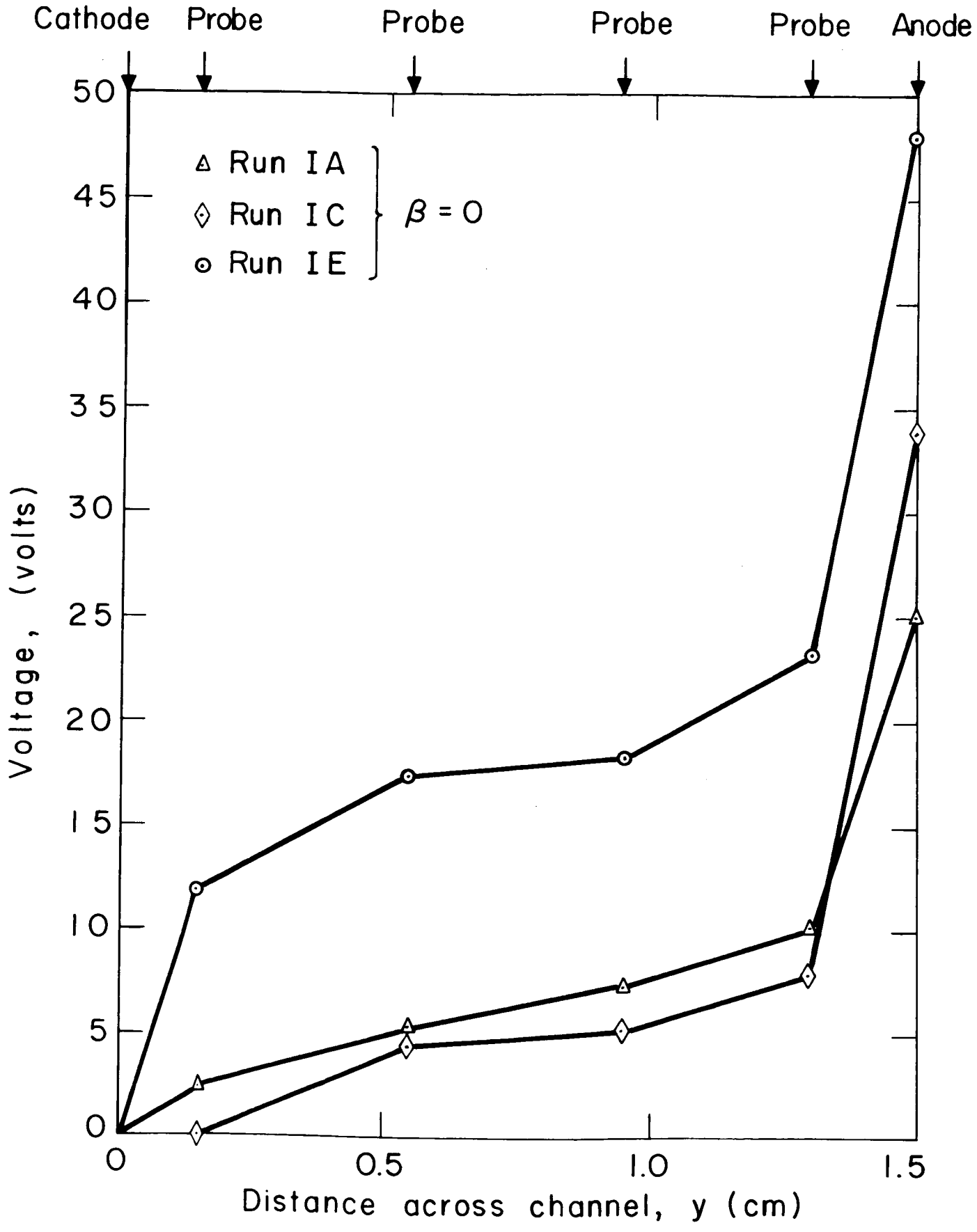

Fig. 6. Typical potential variations across the channel (B = 0) for segmented electrode geometry

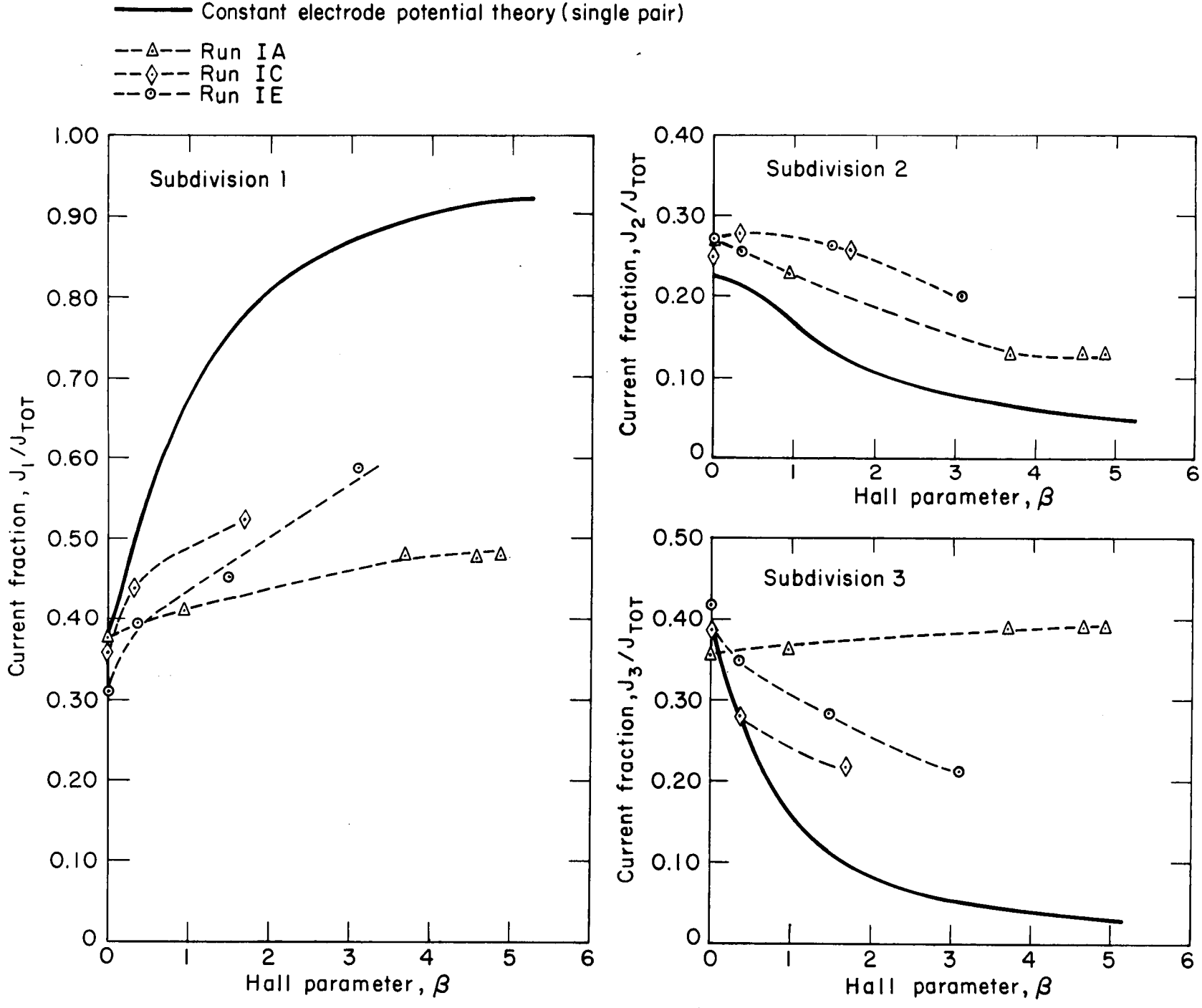

Fig. 7. Current distributions for center electrode pair

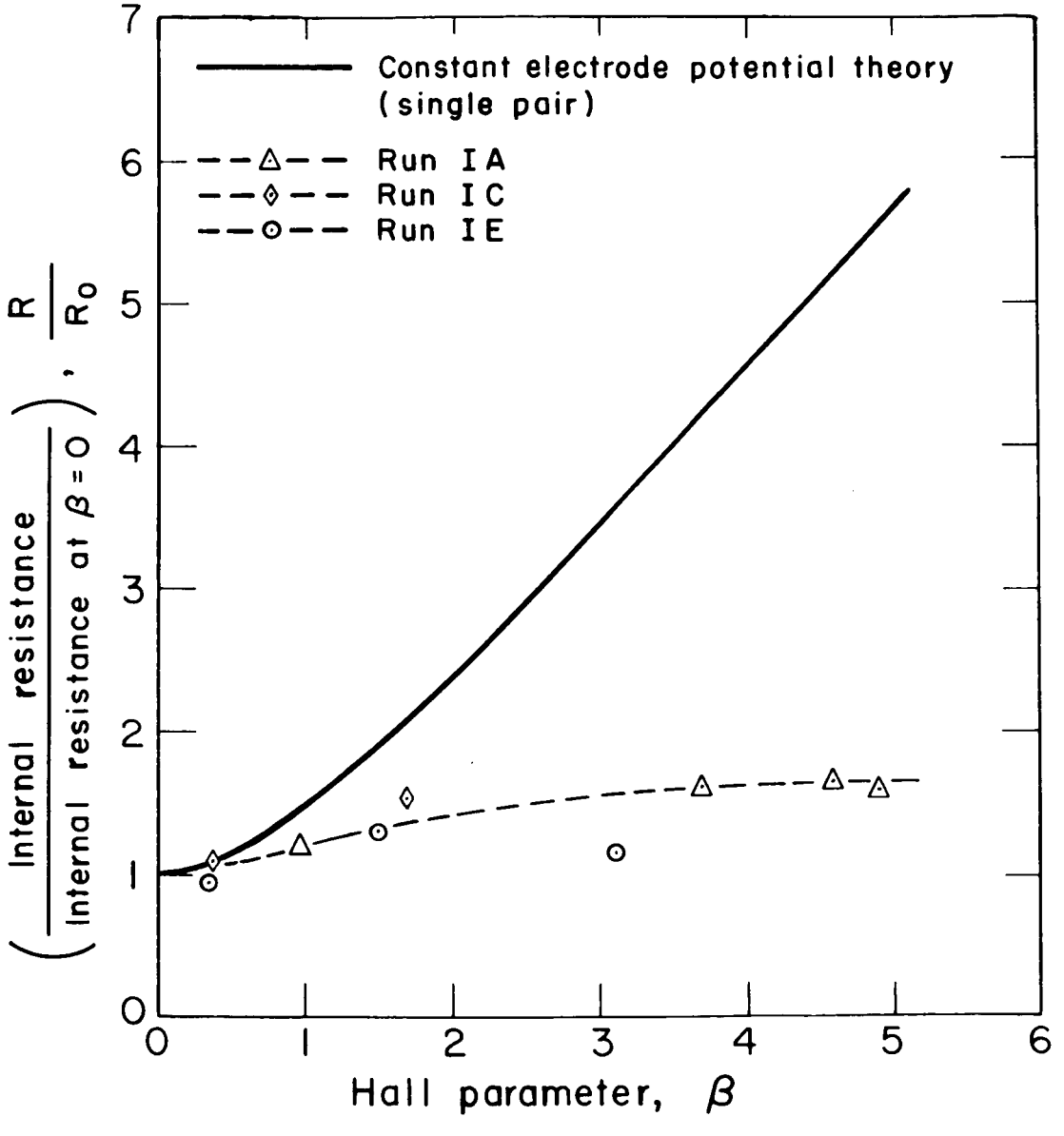

Fig. 8. Effective internal resistance of the center electrode pair

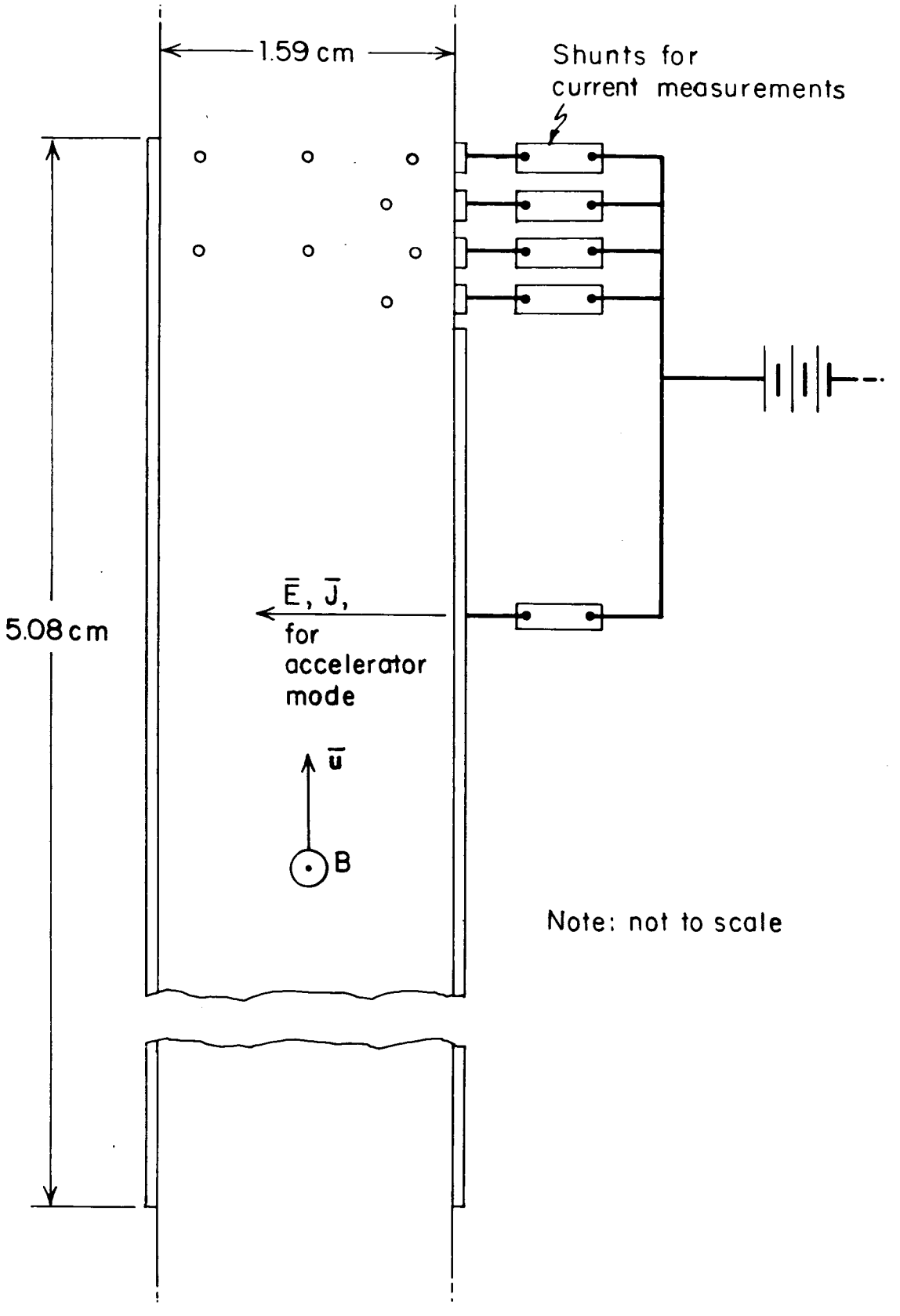

Fig. 9. Continuous electrode test section III

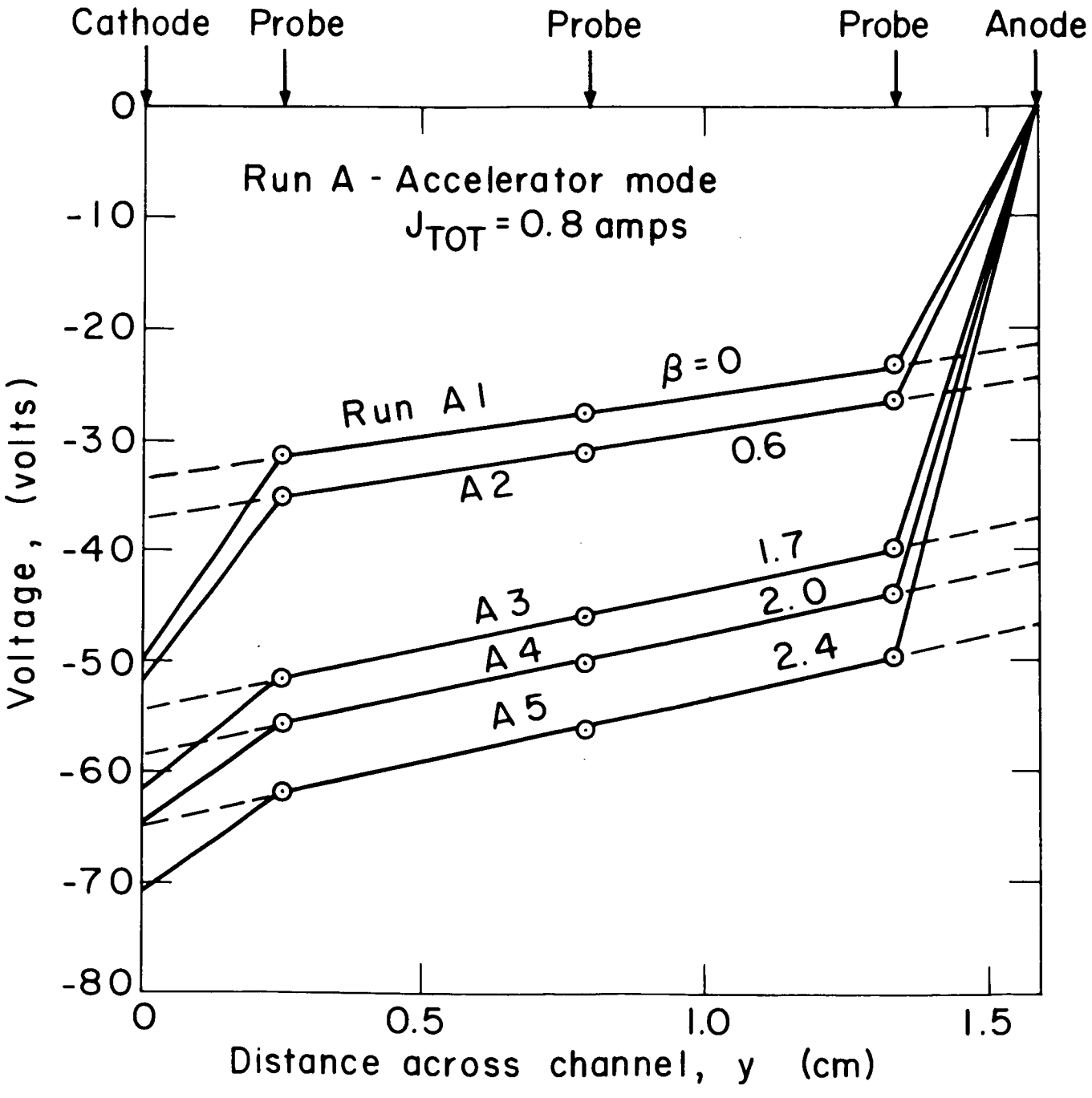

Fig. 10. Typical potential variations across the channel for continuous electrode geometry

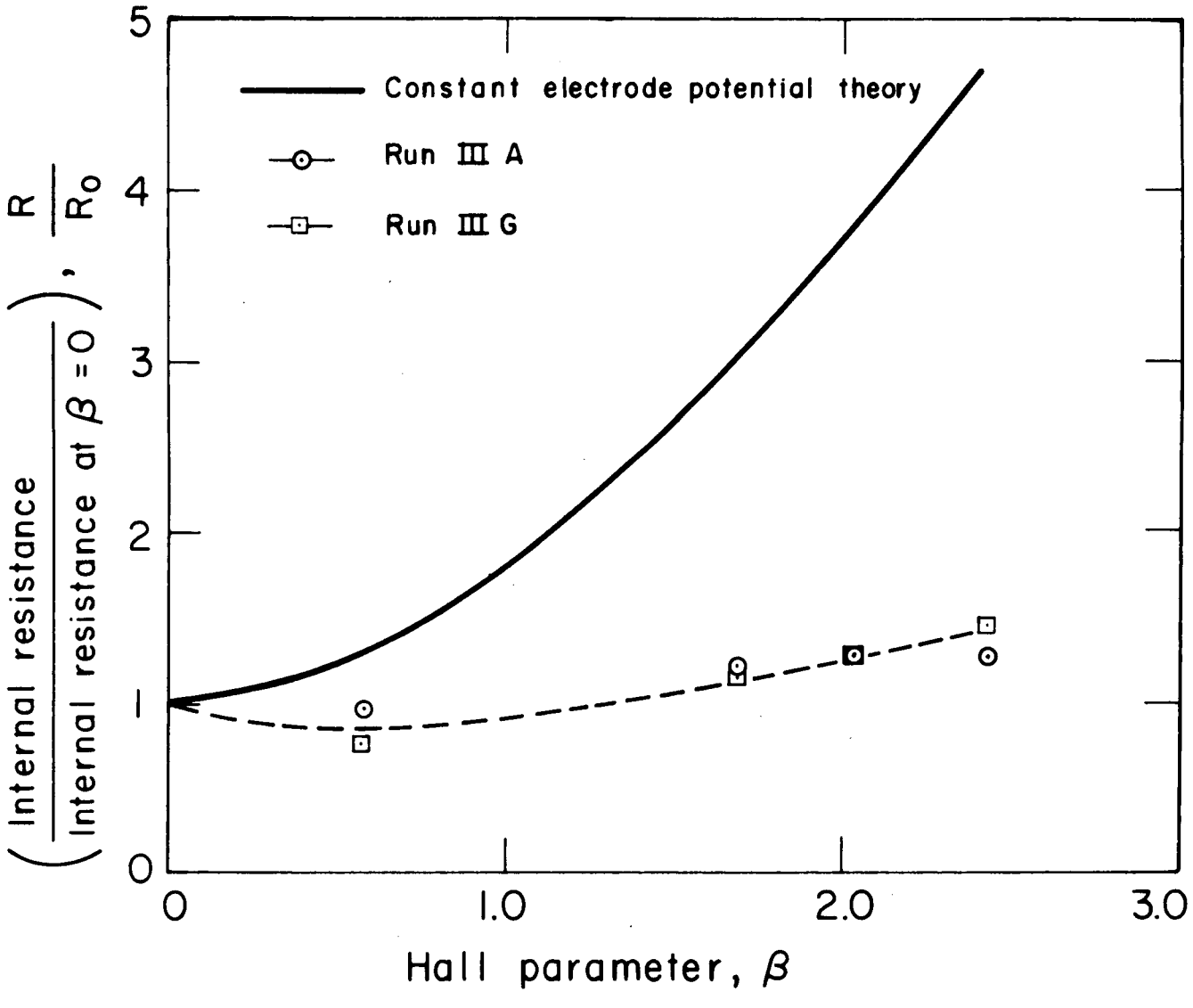

Fig. 11. Effective internal resistance of the continuous electrode pair

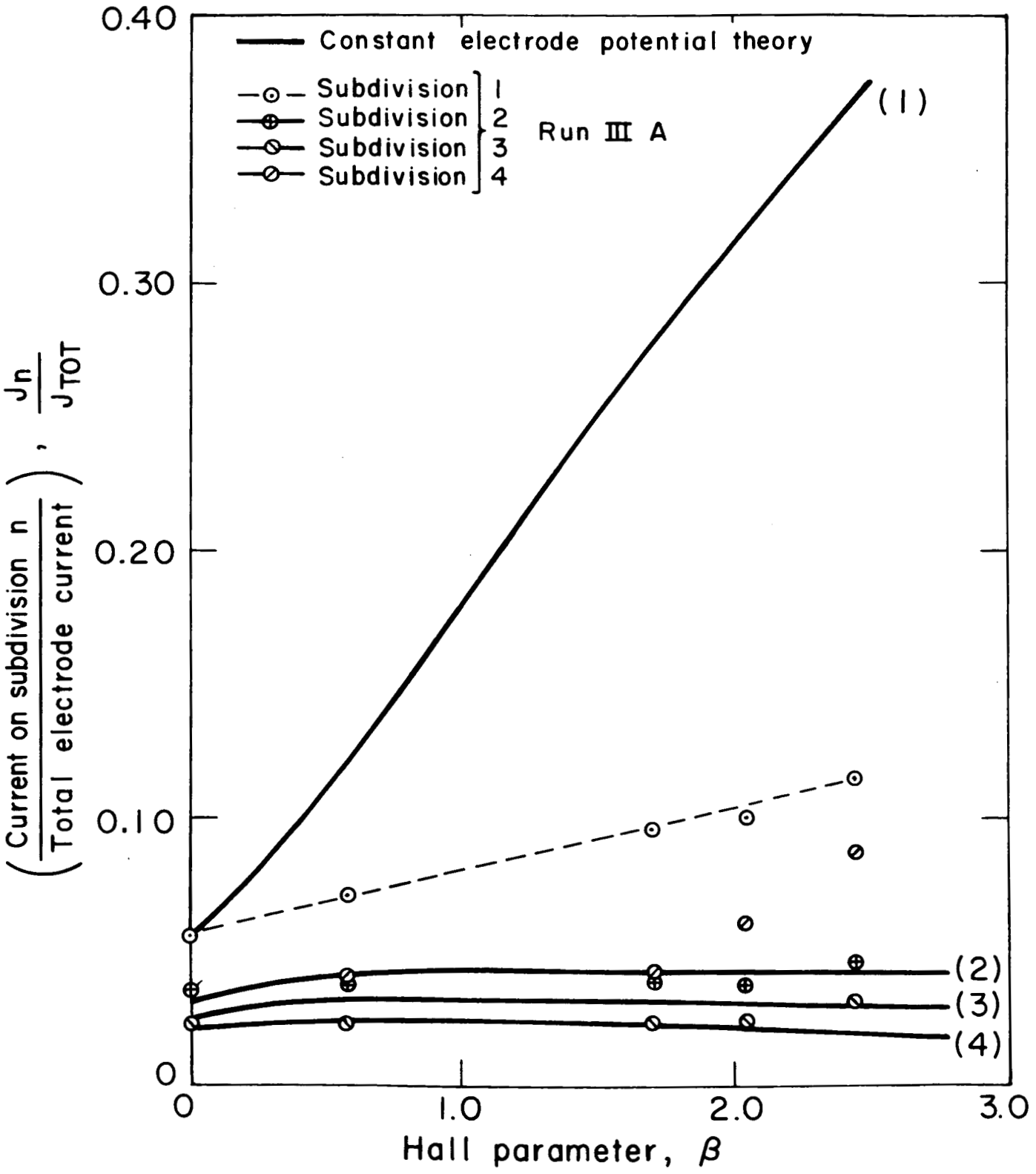

Fig. 12. Current distribution at the exit end of the continuous electrode versus Hall parameter

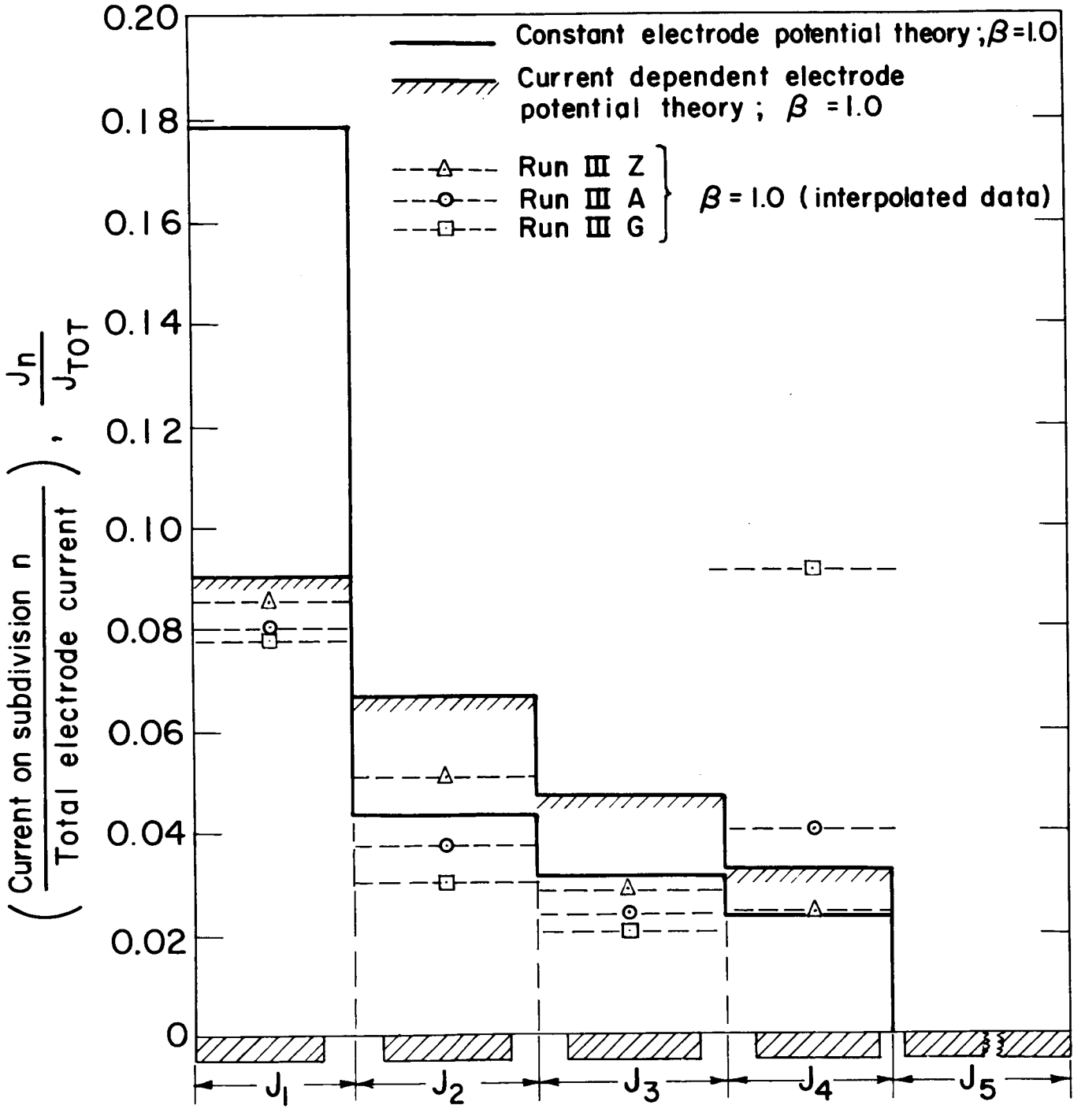

Fig. 13. Current distribution at the exit end of the continuous electrode for Hall parameter, β = 1.0

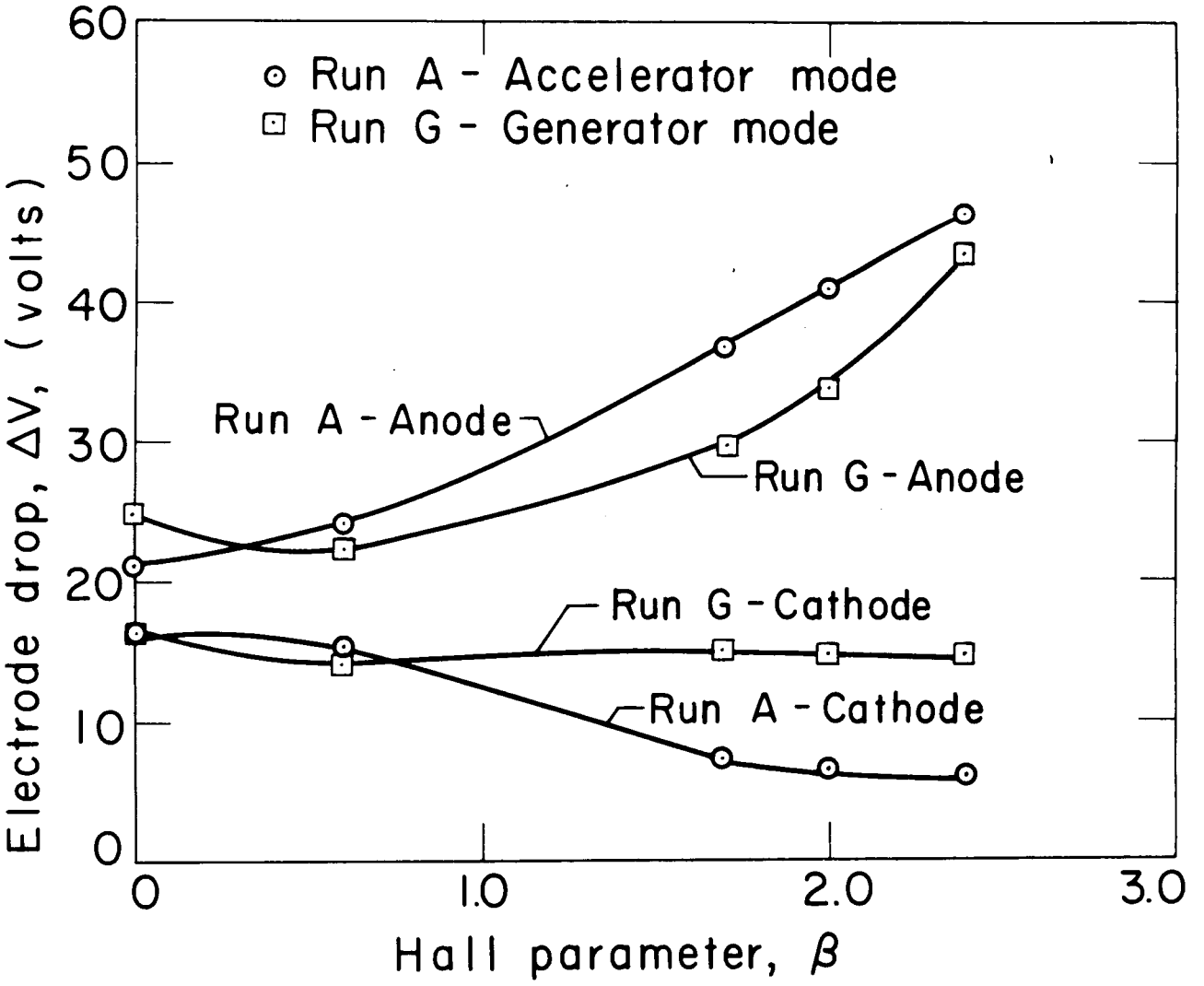

Fig. 14. Variation of anode and cathode potential drops as a function of Hall parameter.